Description and stability of a RPC-based calorimeter in electromagnetic and hadronic shower environments

The CALICE collaboration

J. Apostolakis, G. Folger, A. Ribon, E. Sicking

CERN, 1211 Genève 23, Switzerland

D. Boumediene[a], V. Francais

Université Clermont Auvergne, Université Blaise Pascal, CNRS/IN2P3, LPC, 4 Av. Blaise Pascal, TSA/CS 60026, F-63178 Aubière, France

K. Goto, K. Kawagoe, M. Kuhara, T. Suehara, T. Yoshioka,

Department of Physics and Research Center for Advanced Particle Physics, Kyushu University, 744 Motooka, Nishi-ku, Fukuoka 819-0395, Japan

A. Pingault, M. Tytgat

Ghent University, Department of Physics and Astronomy, Proeftuinstraat 86 (N3), B-9000 Gent, Belgium

G. Garillot, G. Grenier, T. Kurca, I. Laktineh , B. Liu , B. Li, L. Mirabito, A. Steen[1]

Univ Lyon, Univ Claude Bernard Lyon 1, CNRS/IN2P3, IP2I Lyon, F-69622 Villeurbanne, France

R. Été, K. Krüger, F. Sefkow

DESY, Notkestrasse 85, D-22603 Hamburg, Germany

E. Calvo Alamillo, C. Carrillo, M.C. Fouz, H. Garcia Cabrera, J. Marin, J. Navarrete, J. Puerta Pelayo, A. Verdugo

CIEMAT, Centro de Investigaciones Energeticas, Medioambientales y Tecnologicas, Madrid, Spain **F. Corriveau**

Department of Physics, McGill University, Ernest Rutherford Physics Bldg., 3600 University Ave., Montréal, Québec, Canada H3A 2T8

L. Emberger, C. Graf, F. Simon

Max-Planck-Institut für Physik, Föhringer Ring 6, D-80805 Munich, Germany

R. Pöschl

IJCLab, Bât. 100, 15 rue Georges Clémenceau, CNRS / Université Paris-Saclay / Université Paris Cité, 91405 Orsay cedex, France

D.W. Kim, S.W. Park

Seoul National University Hospital, Bundang 13605, Republic of Korea

[a] *Corresponding author*

E-mail: djamel.boumediene@cern.ch

---

[1]Now at National Taiwan University, 10617, Taipei, Taiwan

ABSTRACT: The CALICE Semi-Digital Hadron Calorimeter technological prototype completed in 2011 is a sampling calorimeter using Glass Resistive Plate Chamber (GRPC) detectors as the active medium. This technology is one of the two options proposed for the hadron calorimeter of the International Large Detector for the International Linear Collider. The prototype was exposed in 2015 to beams of muons, electrons, and pions of different energies at the CERN Super Proton Synchrotron. The use of this technology for future experiments requires a reliable simulation of its response that can predict its performance. GEANT4 combined with a digitization algorithm was used to simulate the prototype. It describes the full path of the signal: showering, gas avalanches, charge induction, and hit triggering. The simulation was tuned using muon tracks and electromagnetic showers for accounting for detector inhomogeneity and tested on hadronic showers collected in the test beam. This publication describes developments of the digitization algorithm. It is used to predict the stability of the detector performance against various changes in the data-taking conditions, including temperature, pressure, magnetic field, GRPC width variations, and gas mixture variations. These predictions are confronted with test beam data and provide an attempt to explain the detector properties. The data-taking conditions such as temperature and potential detector inhomogeneities affect energy density measurements but have small impact on detector efficiency.

Contents

1 Introduction

The Semi-Digital Hadronic Calorimeter (SDHCAL) [1] is one of the high-granularity calorimeter prototypes developed by the CALICE collaboration. This technology was optimised for the application of the Particle Flow Algorithm [2] in an collider environment. The SDHCAL is a sampling calorimeter where Glass Resistive Plate Chambers (GRPC) are used as active medium while absorber layers are made of 2 cm thick stainless steel plates. The glass plates have a bulk resistivity of $10^{12}\,\Omega$cm while the surface resistivity is $0.6 - 1\text{M}\Omega/\square$. The anode and cathode thicknesses are 0.7 mm and 1.1 mm, respectively. The gas gap width is 1.2 mm. The geometry of the GRPC is described in Figure 1a. The GRPC is placed inside a stainless steel cassette that plays the role
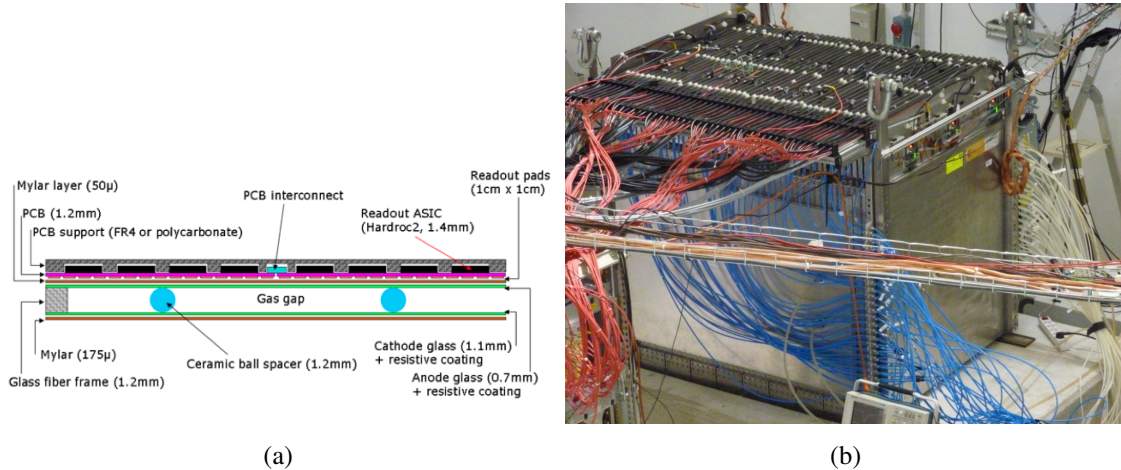
Figure 1: (a) Cross section of a GRPC chamber. (b) The SDHCAL prototype in the CERN SPS area in 2015. The 48 layers are visible on the top side. The right side of the prototype was exposed to the beam.

of a Faraday cage. The longitudinal segmentation is given by 48 GRPC layers interleaved with absorbers, reaching a 1.3 m length and 6 interaction lengths (λ_I). For each layer, the transverse segmentation is governed by the 96×96 charge collection pads of 1 cm^2 each, fine enough to allow track reconstructions [3] and particle identification using machine-learning techniques [4]. The readout pads are isolated from the anode glass by a 50 μm Mylar foil. The charge collected by each pad is measured with a dedicated ASIC [5] that provides a three-threshold readout corresponding to three amplitudes: about 0.1, 5 and 15 pC. The ASIC features a power-pulsing mode [6]. It allows to place the readout electronics in an idle mode between two beam bunch crossings. The active time corresponding to the beam bunch crossing in an ILC-like experiment [7] is expected to last 1 ms every 200 ms. The power-pulsing significantly reduces the power dissipation by a factor 100 to 200 such as no active cooling is needed. The occupency rate is expected to be less than 30 Hz/cm^2 while the GRPC response is considered as stable up to 100 Hz/cm^2 [8].

GRPC are usually used as tracking devices, while in the SDHCAL, we are confronted with a large variety of particles and energies present in a hadronic shower. Furthermore, the high energy density leads to multiple particles inducing a signal in the same pad.

The aim of the multi-threshold approach of the SDHCAL technology is to use the energy density information. The three-amplitude information provided by the detector is sensitive to the event type through the distinction of multiple from single charged particle signal. It was shown that the SDHCAL provides precise energy measurements, especially when exploiting the semi-digital information, allowing to reach a 30% improvement on the energy resolution with respect to a purely digital approach [9]. However, the typical spread of the charge induced by a minimum ionizing particle (MIP) is significant compared to its typical average value. Phenomena that bias the signal induced by the charge avalanches can lead to a sizable change in the balance between the various threshold multiplicities. This paper aims to study the dependency of the SDHCAL response using detailed detector simulations of the prototype (Figure 1b.) and beam test data. Several phenomena

that can affect the detector stability are reviewed.

Section 2 describes the prototype and beam test conditions. The first set of results introduced in this publication is obtained by modeling additional effects in the digitization procedure, based on dedicated avalanche simulations (Section 4). Quantified estimates of the detector stability with respect to different sources of signal bias are provided in Section 5. Section 6 presents a second set of results based on beam test data studies.

2 The SDHCAL Prototype at the CERN SPS beam test

The gas mixture used in the GRPC contains 93% of TetraFluoroEthane ($C_2H_2F_4$), 5% of CO_2, which is a UV quencher gas and 2% of SF_6 which is electronegative gas that absorbs a fraction of the electrons in order to control the avalanche. The electric field is produced with a high voltage of about 6.9 kV.

For 1 m^2 of active layer, 144 HARDROC ASICS [5] collect the signal from 9216 pads that are located on the opposite face of the ASIC electronics board. Each ASIC handles 64 pads. The data are collected by the ASIC until the RAM is full, i.e. until 127 events are recorded as detailed in ref. [9]. In each layer, the acquisition commands are sent to the ASICs by three Detector InterFace (DIF) cards in charge of the data acquisition. A masterboard controls these DIFs and is in charge of the data collection.

The SDHCAL prototype was exposed to beams of muons, electrons and pions during beam test campaigns at the CERN Super Proton Synchrotron (SPS) in 2015. The data acquisition was performed in triggerless mode. The ASIC uses a 5 MHz clock to define a time slot. A time clustering method is used. A time slot containing at least 7 hits is selected. Hits belonging to the adjacent time slots are aggregated to the selected time slot. They define a physical event whose time length is 600 ns [9]. This method is optimised for the rejection of intrinsic noise.

A cooling was needed due to the data-taking cycles at SPS that are longer than those of a full experiment and which limit the impact of the power-pulsing. The lateral sides of the calorimeter were equipped with an ad-hoc 10°C water cooling system.

The atmospheric pressure, as well as the temperature, were monitored during the 2015 data-taking campaigns. The temperature was measured on the outer side of three GRPC chambers as an approximation of GRPC gas temperature. The pressure and temperature variation are averaged over each hour and shown in Figures 2a and 2b, respectively. The temperature variations are noticeable, even during single data runs whose duration is typically two to three hours. A set of data collected within 24 hours is used to study the interplay between the stability of the response and temperature or pressure variations while the detector is operated at a stable high voltage.

3 Data reconstruction

The simulated, as well as the observed events, are reconstructed using the MARLIN framework [10, 11] within the ILC software framework [12]. The time of a hit is recorded and used to reject noise events and to select the fired pads (hits) resulting from the particle interactions with the detector material.
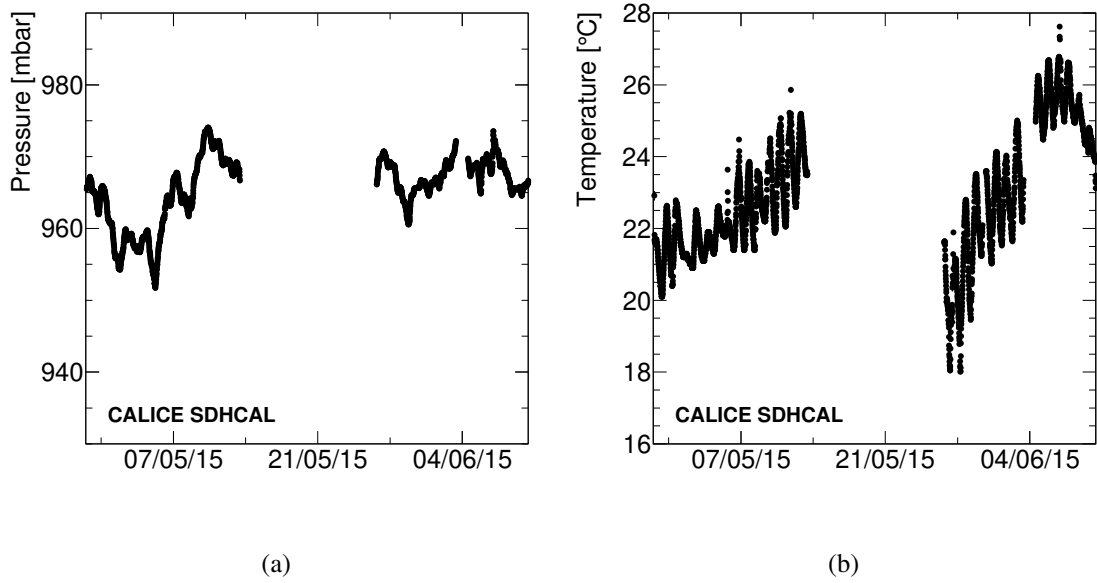
(a)　　　　　　　　　　　　　　　　　(b)

Figure 2: Evolution of the atmospheric pressure ([a](#)) and of the temperature ([b](#)) as measured during the 2015 beam test campaign at CERN SPS.

Several beam energy points, from 7 to 70 GeV were used to study the observed or simulated detector response. Pion showers are selected from the data, and cuts are used to reject electron and muon contaminations. These cuts include a threshold on the number of hits: either no hit or more than three hits per layer. At least 30 layers have to contain a hit. The layer at which the shower starts has to be at the 4th position or more [9]. The high rate of the SPS beam induced efficiency losses that were observed and corrected using a linear function of the time in the spill [9].

The energy is reconstructed using a polynomial technique described in ref. [9]. It uses the amplitude threshold information that makes a software compensation possible. It can also take advantage of the high granularity by including reconstructed tracks [3] and machine learning techniques [4]. The event reconstructed energy, E_{event}, is calculated using the polynomial combination method as follows:

$$E_{\text{event}} = a(N_{\text{tot}}) \times N_1 + b(N_{\text{tot}}) \times N_2 + c(N_{\text{tot}}) \times N_3 \tag{3.1}$$

where N_i is the number of hits exclusively associated to the ith threshold and the factors a, b and c are quadratic functions of the total number of hits, N_{tot}. The factors are adjusted with a χ^2 minimization method such as the reconstructed energies fit to the expected ones:

$$\chi^2 = \sum_{i=1}^{n} \left(E_{\text{beam}}^i - E_{\text{event}}^i \right)^2 / E_{\text{beam}}^i \tag{3.2}$$

where n is the number of events used for the optimisation. The mean reconstructed energy, E_{reco}, and energy resolution, σ_{E}, are obtained from the mean and width of the Gaussian fit to the energy distribution, respectively. In the following, the calibration procedure refers to the measurement of a, b and c from the data or simulated events.

4 Modeling of the detector response

4.1 Simulation of the SDHCAL prototype

The detection process can be summarised by the following steps:

1. Interaction of the primary particle, mainly with the absorber, potentially leading to electro-magnetic or hadronic showers;

2. Interaction of secondary charged particles within the particle shower with the GRPC gas medium leading to the ionization;

3. Charge avalanche development in the GRPCs;

4. Signal induction in the pads;

5. ASIC signal processing;

The first two steps are simulated with the GEANT4 toolkit [13] as described in Section 4.2. The three following ones are modeled with the so-called digitization algorithm described in Section 4.3. Additional corrections of the charge avalanche modeling are extracted from a dedicated simulation and added to the digitizer as described in Section 4.4.

4.2 Simulation of particle interactions with GEANT4

The particle interactions with the detector material are simulated using the version 9.6 of the GEANT4 toolkit, where the full SDHCAL geometry is implemented. The `QGSP_BERT_HP` and `FTFP_BERT_HP` physics lists are used to simulate hadronic and electromagnetic showers. The GEANT4 simulated energy depositions in the detector active volumes are taken as the starting point of the digitization procedure. They are associated with segments of a particle path, so-called steps.

4.3 Digitization algorithm

The digitization algorithm determines the induced charge on each pad for each particle crossing a gas gap. The method is described in detail in ref. [14]. The algorithm proceeds with the selection of the GEANT4 steps as follows:

- rejection of the energy depositions that are created more than $1\,\mu s$ later than the primary particle generation time,

- rejection of steps with a null length,

- random step selection in order to reproduce a given efficiency, ϵ, defined as the fraction of avalanches above the detection threshold of 0.1 pC,

- association of a total induced charge, Q, produced by an avalanche with each energy deposition,

- application of a correction, $A(\theta)$, to the total induced charge, based on the angle θ between the step direction and the GRPC plane, whereby the dependence of A on θ is extracted using muon data [14],

- application of corrections, ρ and ρ', to the total induced charge and to the efficiency based on the avalanche modeling, whereby the dependence of ρ and ρ' on the energy deposit and data-taking conditions is described in Section 4.4,

- a cut-off distance is defined, such as an avalanche development is cancelled if a second avalanche with more charges is present within this distance. This scale is tuned using particle showers to reproduce the observed multiplicities [14],

- distribution of the charges over the pads.

The amount of induced charges, Q, is used to populate the three-amplitude categories following three thresholds: 0.1, 5 and 15 pC. A charge Q_0 is first modeled by a Polya distribution [15] using the data:

$$P(Q_0) = \frac{1}{\Gamma(1+\delta)} \left(\frac{1+\delta}{\bar{Q}} \right)^{1+\delta} Q_0^{\delta} e^{\left[\frac{-Q_0}{\bar{Q}(1+\delta)} \right]} \qquad (4.1)$$

where Γ is the Gamma function. $\bar{Q}$ and δ are the average charge and the width of the charge distribution. They are derived from dedicated high energetic muon beams with a threshold scan method [14]. The remaining parameters of the digitization are tuned in order to reproduce the number of hits observed in electromagnetic showers.

The simulated charge, including all the corrections, is given by:

$$Q_{\mathrm{MC}} = Q_0 \times \rho \times A(\theta) \qquad (4.2)$$

Similar correction, ρ', is applied to the efficiency:

$$\epsilon_{\mathrm{MC}} = \epsilon_0 \times \rho' \qquad (4.3)$$

where ϵ_0 is the efficiency measured using high energetic muon beams.

The digitization procedure was tuned for isolated tracks or showers. The impact of two consecutive showers on the performance of the detector is neglected due to the low expected particle rate. Moreover, it was assumed that the variations modelled in the next Section, can be factorised, i.e., ρ is independent from Q. Q_0 is measured from the data and can be updated separately.

4.4 Simulation of the avalanches

The mathematical distribution used to predict the GRPC signal in ref. [14] oversimplifies and neglects some physical processes that will be considered for the first time in this study. The Monte Carlo simulation of the avalanche described in this section provides corrections applied hit by hit to the charge Q_0 and to the efficiency in the digitization procedure. The charge correction ρ is defined by:

$$\rho = \frac{< Q(\Delta C) >}{< Q(\mathrm{nominal}) >} \qquad (4.4)$$

where ΔC represents a variation in data-taking condition (e.g. temperature or the energy deposit), $< Q >$ is the average of the total induced charge estimated using the full avalanche simulation described in this section. The properties of the GRPC that are taken into account for the avalanche simulation are listed in Table 1. They are used to define $< Q(\mathrm{nominal}) >$.

The implementation of the avalanche simulation is described in refs. [16, 17] and adapted to the SDHCAL properties. This Monte Carlo simulation models the amplitude and the efficiency.

Table 1: Avalanche simulation parameters with their nominal values. ϵ_0 refers to the vacuum electric permitivity.

Parameter		Value
Width	Gap	0.12 cm
	Anode	0.07 cm
	Cathode	0.11 cm
Permitivity	Anode	$7\epsilon_0$
	Cathode	$7\epsilon_0$
Gas Mixture	$C_2H_2F_4$	93%
	CO_2	5%
	SF_6	2%
Electric Field		57500 Vcm^{-1}
Temperature		293.15 K
Pressure		1 atm

4.4.1 Primary ionization

When running the complete digitization of SDHCAL, the primary ionization is described by GEANT4 in terms of energy deposits. In order to have an event-by-event simulation of the electron distribution in the gas, the HEED simulation program is used [18]. Primary and secondary ionisations are simulated by HEED including emissions of photo-electron and auto-ionization Auger electrons. About 8 charge clusters are typically produced per mm in the GRPC when a charged particle traverses it, containing 21 electrons in average.

The correlation between the number of ionisation electrons and energy deposit for the gas mixture used in the SDHCAL prototype is determined with the HEED package. An average energy of 29.5 eV is required for an electron-ion pair production. In the digitization process, this value is used to associate a number of ionisations with each GEANT4 step.

4.4.2 Electronic avalanche

The electric field induces the electron drift towards the anode in the GRPCs. An electron avalanche is the consequence of the charge multiplication in the GRPC while the electrons interact with gas molecules. This phenomenon is described in the simulation using the Riegler-Lippman-Veenhof model [19].

Two coefficients are used to characterize the avalanche development: the Townsend coefficient, α, and the attachment coefficient, η.

Three additional parameters are considered: the electron drift velocity, the longitudinal and the transverse diffusion coefficients. The drift velocity and the diffusion amplitude account for the avalanche development. The diffusion has a significant impact on the amplification process as it increases the average charge path.

Before each avalanche simulation, for each condition of temperature, pressure, and gas composition, the coefficients α, η, the electron velocity and diffusion parameters are estimated using the Magboltz 9.01 package [20]. They are mapped as a function of the electric field value. Since the electric field is a function of the position in the gas gap and a function of time, these parameters will also vary depending on the position and time as detailed below.

The avalanche is simulated in a gas gap divided into longitudinal intervals of 0.5 μm each. The average number of electrons in each interval is governed by the coefficients and the initial number of charges. The average number of electrons, $\bar{n}(x)$, and ions, $\bar{p}(x)$, produced by one electron after a step of lengh x are modeled as follows

$$\bar{n}(x) = e^{(\alpha-\eta)x} \tag{4.5}$$

and

$$\bar{p}(x) = \frac{\alpha}{\alpha - \eta}(e^{(\alpha-\eta)x} - 1) \tag{4.6}$$

An iterative procedure is used to estimate the number of charges in each detector interval until all the electrons have reached the anode, after 4500 iterations in average [1]. The evolution of the number of electrons is given by

$$n(x) = \begin{cases} 0, & s < k\frac{\bar{n}(x)-1}{\bar{n}(x)-k} \\ 1 + \ln\left(\frac{(\bar{n}(x)-k)(1-s)}{\bar{n}(x)(1-k)}\right)\frac{1}{\ln\left(1-\frac{1-k}{\bar{n}(x)-k}\right)}, & s > k\frac{\bar{n}(x)-1}{\bar{n}(x)-k} \end{cases} \tag{4.7}$$

where s is a random number $\in [0, 1)$ from the uniform distribution and $k = \eta/\alpha$.

The diffusion of each electron is simulated at each iteration.

The electrons that reach the resistive anode lead to an accumulation of charges at the surface of the anode. Their relaxation time is higher than the avalanche development time. The space charge effect is estimated while the influence of the charges produced in the avalanche on the electric field is computed. The numbers and positions of electrons or ions, number of electrons on the anode, combined to the applied electric field are used to compute the electric field as a function x at each time iteration. Any change in the electric field requires the various coefficients to be updated, especially α and η.

Finally, the induced current is computed using Ramo's theorem generalized to resistive materials accounting for the properties of the resistive layers [19]. The transverse profile of the avalanche is assumed to be negligible compared to the pad size. While the avalanche simulation predicts a total signal induced by a given avalanche, the digitization procedure models its distribution on multiple pads. This modeling of the avalanches does not describe the signal in regimes with very high number of charges like streamers.

4.4.3 Simulation output

The main outputs of the avalanche simulation are:

- the total induced charge, Q, at the level of the pads. For the stability studies, only the relative variation of the mean values of Q are used;

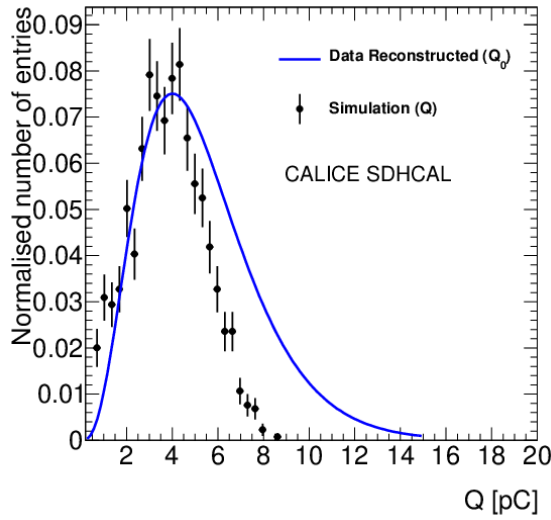[1]The avalanche simulations used in this paper required 10^4 CPU hours.

Figure 3: Distribution of total induced charge for a simulated RPC (dots). The total induced charge was reconstructed from the data using the threshold scan method assuming a Polya distribution and describes all the channels of the prototype. The simulation assumes a homogeneous detector at nominal conditions.

- the efficiency, ϵ;

- streamer probability: an empirical and raw way to estimate the streamer probability is to monitor the fraction of simulated events for which the amplification exceeds a factor of $e^{22} \simeq 4.85 \times 10^8$ [15, 21].

The number of electron charges produced in the avalanches is about 15 pC on average, while the total induced charges are 3.7 pC on average. The induced current reaches a maximum after about 11 ns. The distribution of simulated Q is compared to Q_0 reconstructed from the data and shown in Figure 3. Q_0 is the superimposition of the different channels, thus combining different readout channels and different planes. The overall amplitude of Q is coherent with the measured one and the spread observed in the data is due to the inhomogeneity of the detector channels.

5 Predicted Stability of the SDHCAL Prototype Response

Instabilities in the prototype response to electromagnetic or hadronic showers have been reported in ref. [9]. These variations are seen between different shower types, between different data taking periods, between different layers or even inside the same chamber. In this section, several effects that can induce variations in the detector response are reviewed using simulations. Some are related to the calibration method (use of high energy muons to model the avalanche in the digitizer), some are related to intrinsic properties of the prototype (GRPC gap homogeneity) or data taking conditions (temperature, pressure, magnetic field, gas mixture). In order to estimate the impact of each effect on the number of hits, a Monte Carlo simulation of electrons, pions and muons is produced. The
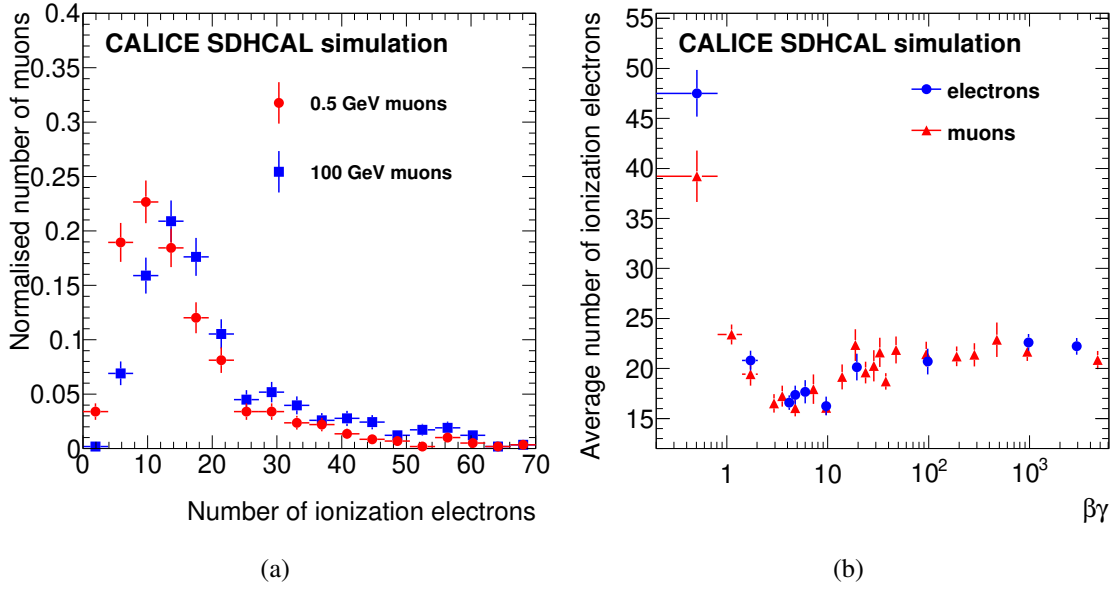
Figure 4: (a) Normalized distribution of number of ionisation electrons produced in the gas mixture by 0.5 and 100 GeV muons. (b) Average number of ionisation electrons produced in the gas mixture by electrons or muons as a function of the Lorentz factors $\beta\gamma$.

effects described in this section are modeled using the avalanche simulation technique described in Section 4.4 and summarized in terms of variations in the mean total induced charge and efficiency. These two variations are used to scale the charge and efficiency in the digitization procedure described in Section 4.3 when producing the full Monte Carlo simulation of the SDHCAL response to electron or pion showers.

5.1 Universality of the MIP-based calibration

For a given type of particles, the energy deposit in the GRPC gas mixture depends on their momenta and fluctuates from one interaction to another. Figure 4a illustrates the distribution of the number of ionization electrons created by 0.5 and 100 GeV muons. Typically, an average of 15 electrons are created in the SDHCAL chamber due to ionization. A systematic difference between the two distributions is observed.

As shown in Figure 4b, the number of electrons (and ions) created in the gas mixture follows the Bethe-Bloch formula [22]. Ideally, the total induced charge measured after the avalanche should not depend on the properties of the MIP. A possible dependence on the number of initial charges, and therefore on the energy and type of the charged particle that ionized the gas mixture, is investigated. The digitizer charge distribution is tuned using the average response of the GRPCs to 100 GeV muons. The relative response of a GRPC to these muons with respect to the GRPC response to low energetic charged particles[2] thus has to be estimated. This relative response can be used to

---

[2]The typical energy of interacting charged particles in an electromagnetic or hadronic shower covers a large scale from hundreds of keV to GeV.

extrapolate the muon calibration to any particle type or energy or estimate the bias induced by this modeling.

Electron and muon induced avalanches are generated using different momenta values from 100 keV to 500 GeV. The overall dependence of the total induced charge on the number of ionisations is shown on Figure 5a. For a number of initial electrons greater than 20, a plateau is observed. In this saturated regime, the total induced charge does not depend on the number of ionisations. Below 10 electrons, a significant drop is observed. Furthermore, the probability that an avalanche reaches the detection threshold is expressed in terms of efficiency and is shown on Figure 5b. An efficiency plateau is reached above 10 electrons. For example, the efficiency is 66% on average if the incoming charged particle creates 3 electrons by ionising the gas mixture.

(a) (b)
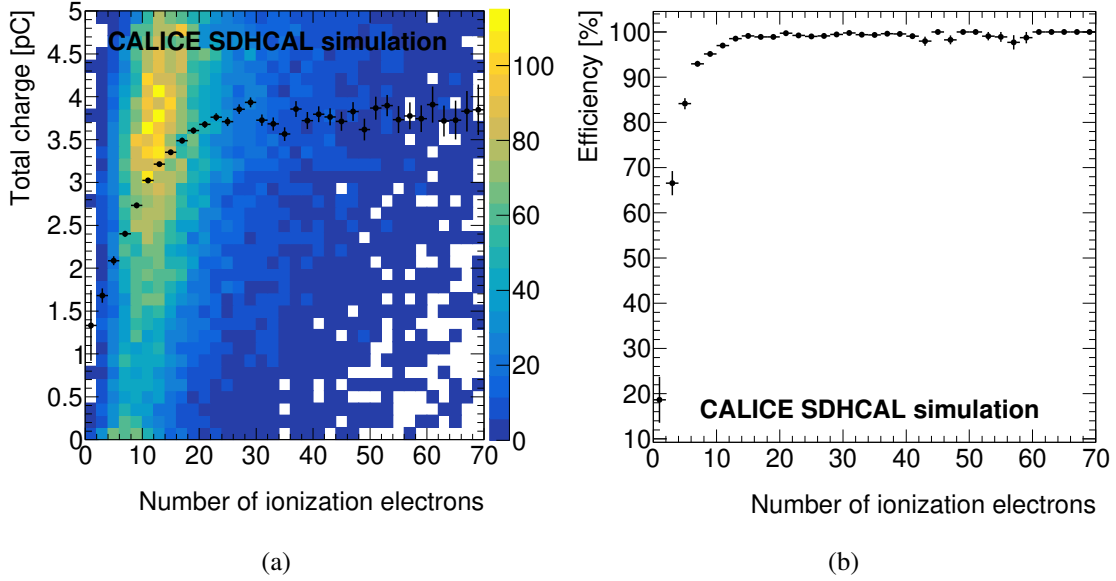
Figure 5: Total induced charge (a) and efficiency (b) induced by an avalanche as a function of the number of ionisation electrons produced in the gas mixture by the ionizing particle. Total induced charge is averaged on each bin and shown as black dots in (a).

The dependence of the total induced charge on the initial number of ionisations is used to model a correction, $\rho(E/E_0)$ defined as

$$\rho(E/E_0) = \frac{<Q(E/E_0)>}{<Q(\text{nominal})>} \tag{5.1}$$

where E is the energy deposit associated to a given GEANT4 step, E_0 is equal to 29.5 eV (section 4.4.1), $<Q(E/E_0)>$ is the average total induced charge derived from Figure 5a and $<Q(\text{nominal})>$ is the average total induced charge expected for 100 GeV muons under nominal conditions. This correction extrapolates the 100 GeV muon Polya calibration to the variety of particles that are detected by the GRPC, especially in electromagnetic and hadronic showers. A correction is also defined for the avalanche efficiency:

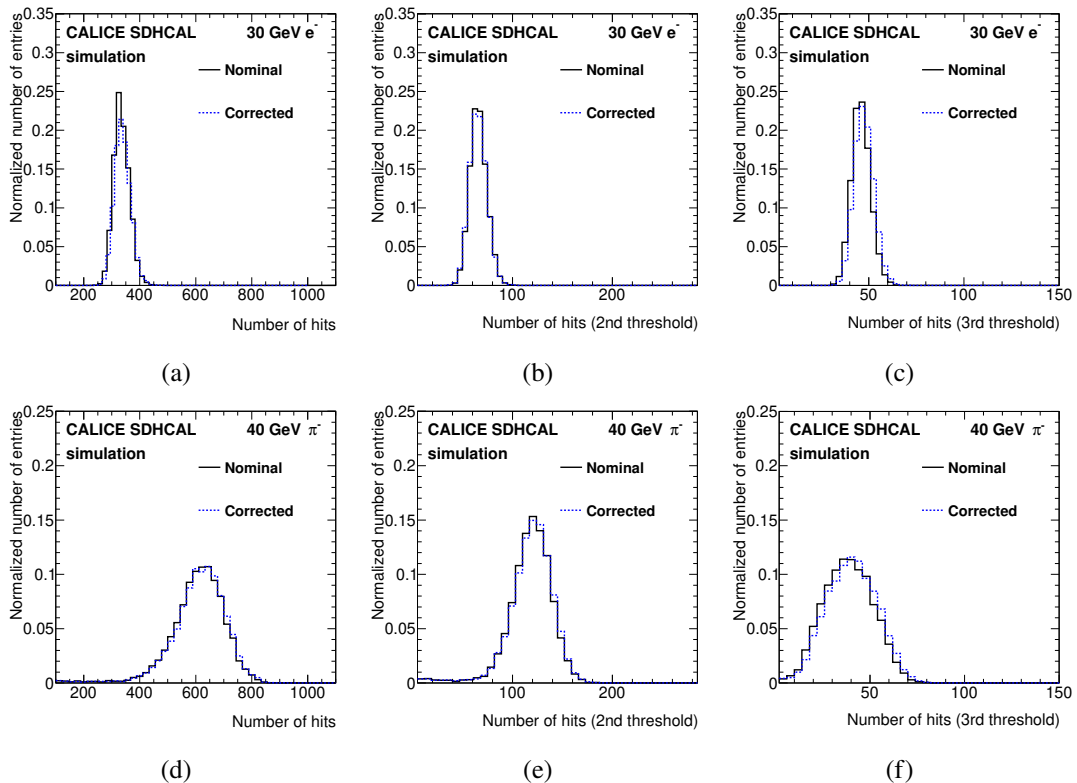$$\rho'(E/E_0) = \frac{\epsilon(E/E_0)}{\epsilon(\text{nominal})} \tag{5.2}$$

Figure 6: Distribution of the number of hits passing the first threshold at 0.1 pC (a,d), the second threshold at 5 pC (b,e) and the third threshold at 15 pC (c,f) for simulated 30 GeV electrons (top) or 40 GeV pions (bottom). The full GEANT4 simulation was performed with digitization modeling that does not account for energy deposit in the GRPC gas (solid black histogram) or a modeling that accounts for it (dashed blue histogram).

where $\epsilon(E/E_0)$ is the efficiency derived from Figure 5b and ϵ(nominal) is the efficiency expected for 100 GeV muons under nominal conditions.

This correction addresses potential mismodelings of the avalanche, leading to a bias on the reconstructed energy in the simulation depending on the type of shower. In order to estimate the simulation bias, the full digitization procedure described in Section 4.3 is applied. It is completed with the efficiency and amplitude correction described above which takes as input GEANT4 step energies. The impact of this correction on the average number of hits is estimated and is shown in Figure 6. The relative variation of the average total number of hits is typically 1% for both electrons and pions as well as the average number of hits passing the second threshold. For the third threshold this variation is 2.9 ± 0.5 % (5.3 ± 0.5 %) for electrons (pions).

The energy reconstruction is tuned, using the polynomial combination method. The factors a, b and c from eq. (3.1) are adjusted with a χ^2 minimization method as given in eq. (3.2). These factors are extracted using simulations of electron (or pion) showers with energy deposit correction. They are used to reconstruct the electron (or pion) energies in the simulation with and without energy deposit correction in an energy range of 7 to 70 GeV. The largest variation in the reconstructed
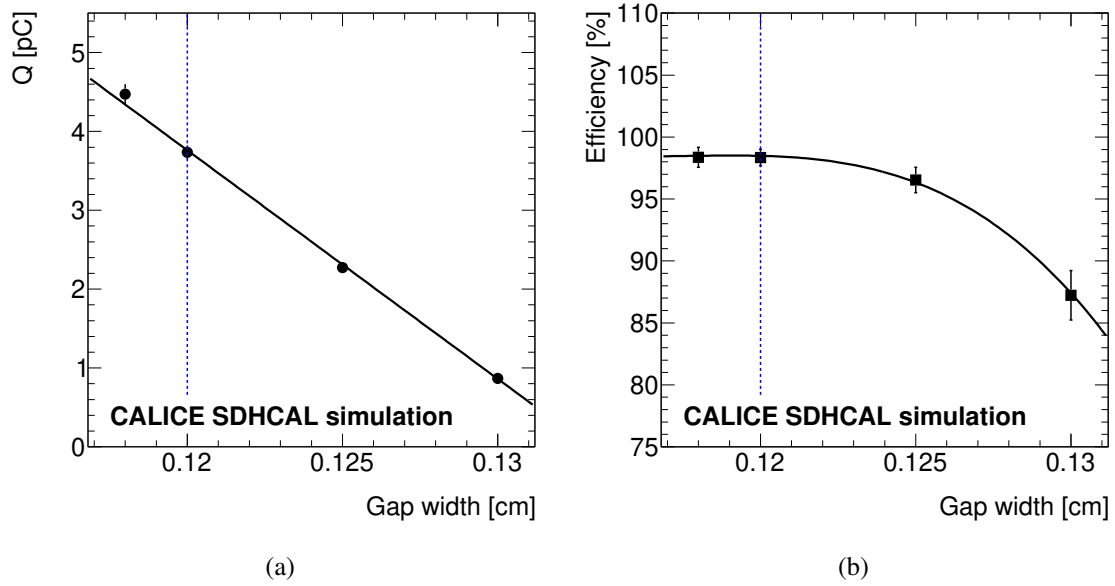
(a)   (b)

Figure 7: Mean total induced charge (a) and efficiency (b) as a function of the gap width for hits initiated by simulated 100 GeV muons. The nominal gap width is indicated by a vertical dashed blue line. The function that fits the variation is represented by a black solid line.

energy is 4% for electromagnetic showers and 2% for hadronic showers. In the following, the dependence on the energy deposit is included in the digitizer algorithm.

5.2   Impact of mechanical homogeneity

The SDHCAL design is challenging due to the large number of GRPC plates and their large size. The large-scale prototype is produced with a tolerance of 40 μm on the thickness of the individual GRPC plates. Variations in the GRPC gap width have a direct impact on the avalanche development and can lead to inhomogeneous efficiencies or signal amplitudes. A gap width deformation would lead to two opposite effects: a variation in the charge path and therefore of the charge multiplication and a variation in the electric field. In order to quantify the impact of a potential gap width inhomogeneities on the avalanche production process, different geometries are simulated using 100 GeV muons. The high-voltage is assumed to be stable and the gap width variations are then propagated to the electric field.

The signal induced in the GRPC increases significantly for smaller gap sizes. Figure 7a shows the evolution of the total induced charges as a function of the GRPC gap width. Above 0.12 cm, the nominal thickness of the SDHCAL GRPC gaps, a sizable loss of signal is expected. A gap deformed by +50 μm will lead to a reduction of the signal amplitude of about 38%. Such a variation will induce a significant effect on the second and third threshold hit multiplicities. The hit efficiency, defined as the fraction of ionizations that induce a signal above the first threshold, is estimated as a function of the gap width (cf. Figure 7b). It decreases in the case of gap inflation. An efficiency loss of about 1% (2%) is expected if the GRPC gap is deformed by +10 μm (+50 μm).

In order to estimate the dependence of the detector response regarding gap width variations, a full simulation of electron and pion showers is produced. Particles with energies from 7 to 70 GeV interacting in the SDHCAL are simulated. In order to account for the effect of a gap width variation, the dependence of the efficiency and the signal amplitude on the gap width is interpolated using Figures 7a and 7b. This dependence is implemented in the digitization step of the simulation.

Different detector geometries are compared: the nominal geometry and pessimistic scenarios where the GRPC gaps are inflated following different values, from 10 to 50 μm. It is assumed that all the detector layers are deformed coherently (referred to as "+10 μm"). An alternative scenario is considered where the gap chambers are randomly varied following a flat distribution from −100 μm to +100 μm (referred to as "±100 μm"). In this case, the deformation of each layer gap is kept constant in all Monte Carlo events to model an intrinsic design inhomogeneity. The chosen value of 100 μm is pessimistic regarding the tolerance of 40 μm imposed on the design of each GRPC plate.

The number of hit distributions are reported on Figure 8 for the nominal geometry and for a +10 μm inflated gap using electrons and pions. A gap width variation of 10 μm leads to a drop of 3% in the average hit number. When considering the second and third threshold hit multiplicities, the drops are about 6% and 8%, respectively.

The ±100 μm tolerance scenario leads to a loss in the expected number of hits. Even though the width variations sum to zero on average, the effect on the number of hits is significant. This is explained by threshold effects and the non-linear dependence of the efficiency on the gap width. Moreover, such a random width variation induces a layer-to-layer smearing of the detector response.

Although the overall number of hits is relatively stable, the variation of high amplitude hits will affect the performance of the SDHCAL, where the energy reconstruction benefits from the shower density information provided by the second and third threshold hits. In order to estimate the stability of the reconstructed energy as a function of the detector gap deformation, the entire reconstruction procedure is applied to simulated pion showers at various beam energies, from 7 to 70 GeV. The a, b and c parameters from eq. (3.2) are computed for both types of showers and different configurations. Figure 9 illustrates the dependence of these factors on the gap width. Only the variations in the c factor value is significant.

Two scenarios are considered:

- The energy calibration is performed on a given detector geometry, then data are collected after a gap width variation: the energy bias and the loss in resolution induced by this case is obtained by applying the nominal reconstruction factors, i.e., calibrated on the nominal geometry, on events simulated with a deformed geometry.

- The detector geometry is different from the nominal one but stable and known: in this case, the energy reconstruction factors are derived from and applied to each geometry.

In the first scenario, if the detector chambers are coherently inflated by +10 μm, the reconstructed energy is shifted by 5% to 17% when considering 7 to 70 GeV pion showers (cf. Figure 10a).

If the energy determination is adapted to the deformed geometry (second scenario), the new a, b and c factors absorb the hit multiplicity changes and restore the linearity within ±5% (cf. Figure 10b). When considering a tolerance of ±100 μm, the layer-to-layer gap width variation
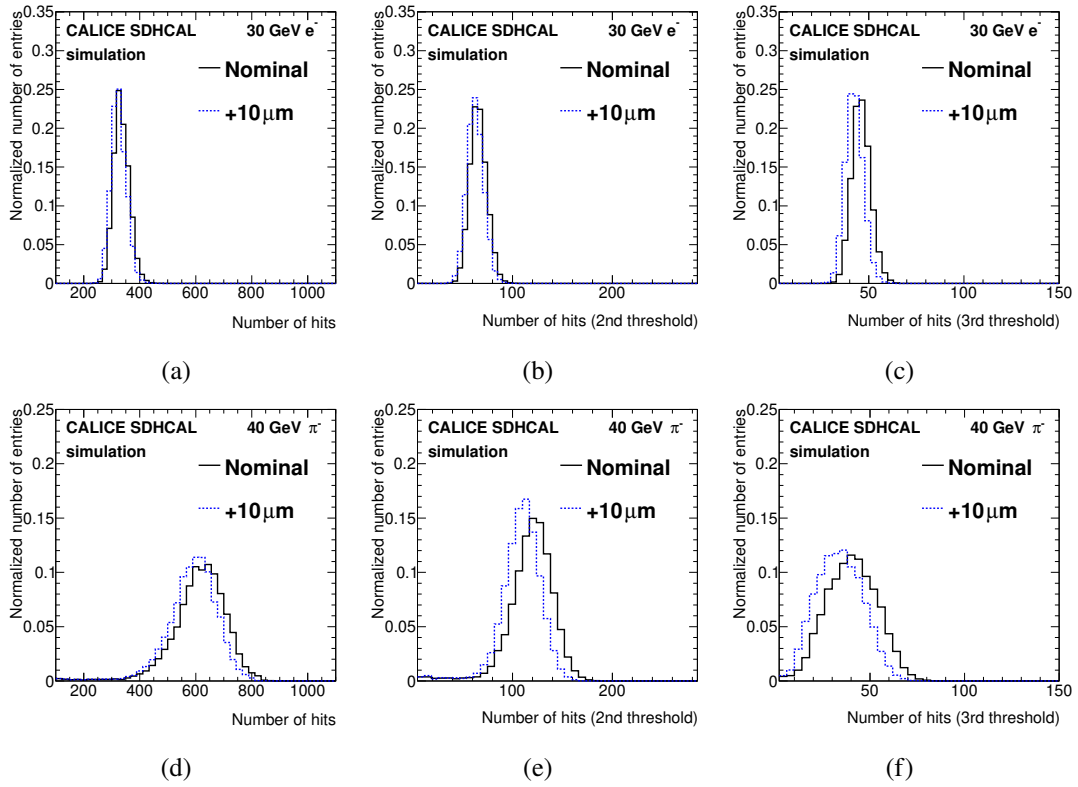
Figure 8: Distribution of the number of hits passing the first threshold at 0.1 pC (a,d), the second threshold at 5 pC (b,e) and the third threshold at 15 pC (c,f) for simulated 30 GeV electrons (top) or 40 GeV pions (bottom). The full GEANT4 simulation was performed with digitization modeling using the nominal geometry (solid black histograms) or a geometry where the gaps are coherently inflated by +10 μm (dashed blue histogram).

translates into a spread in the reconstructed energy the *a*, *b* and *c* factors cannot absorb. The worsening of energy resolution by about 2% is observed as shown in Figure 11.
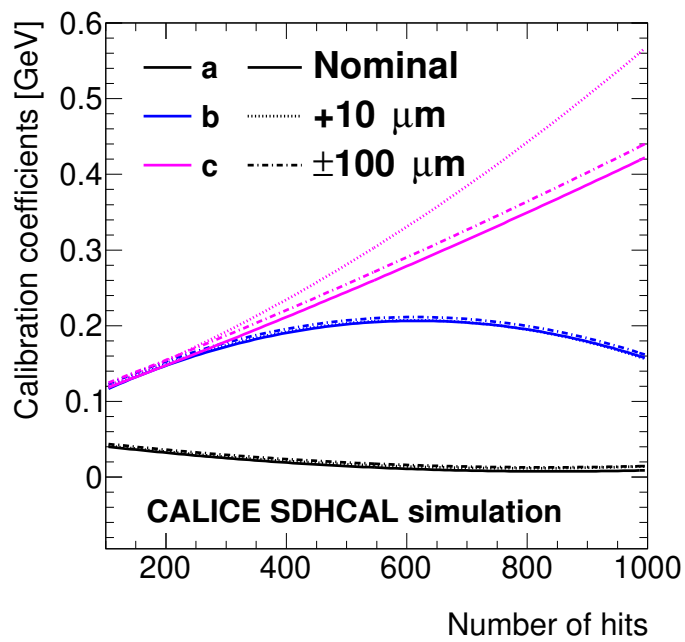
Figure 9: Dependences of the a, b and c energy reconstruction factors on the number of hits. The factors are determined from a simulated sample of pion showers using the nominal geometry (solid lines), geometry with coherent gap inflation by $+10\,\mu m$ (dotted lines) and geometry with random gap variations by $\pm100\,\mu m$ (dash-dotted lines).
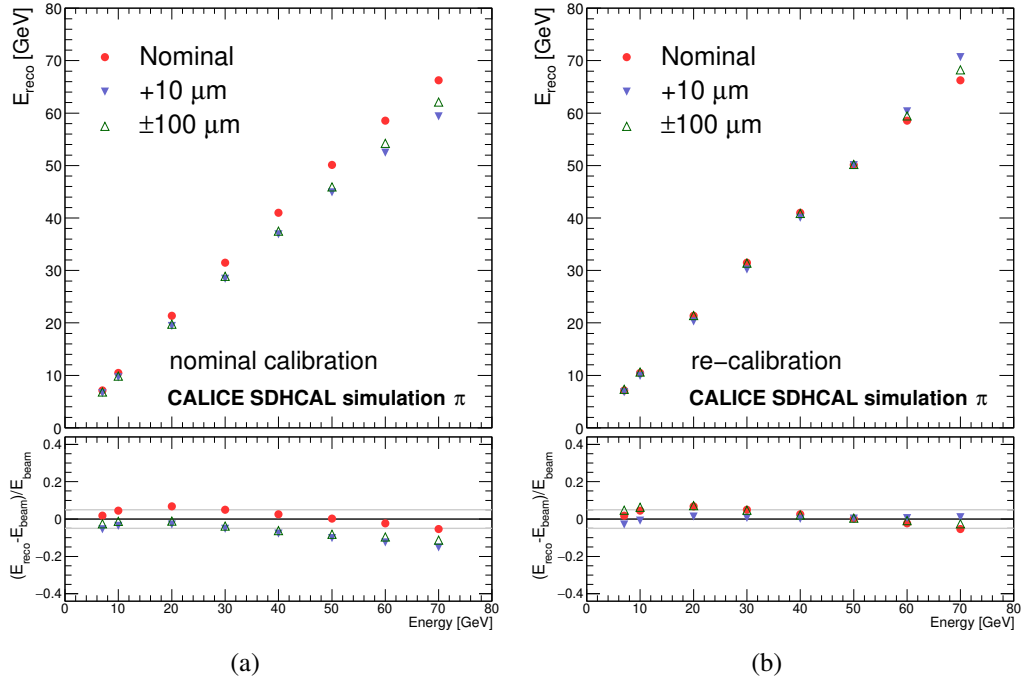
Figure 10: Pion reconstructed energy as a function of the generated energy for simulations using nominal gap (red circles), coherent gap variation by $+10\,\mu m$ (blue filled triangles) and random gap variation by $\pm100\,\mu m$ (green open triangles). For each of the three simulation options, the energy reconstruction factors are optimised using the nominal simulation for all cases or (a) re-calibrated for each geometry (b).
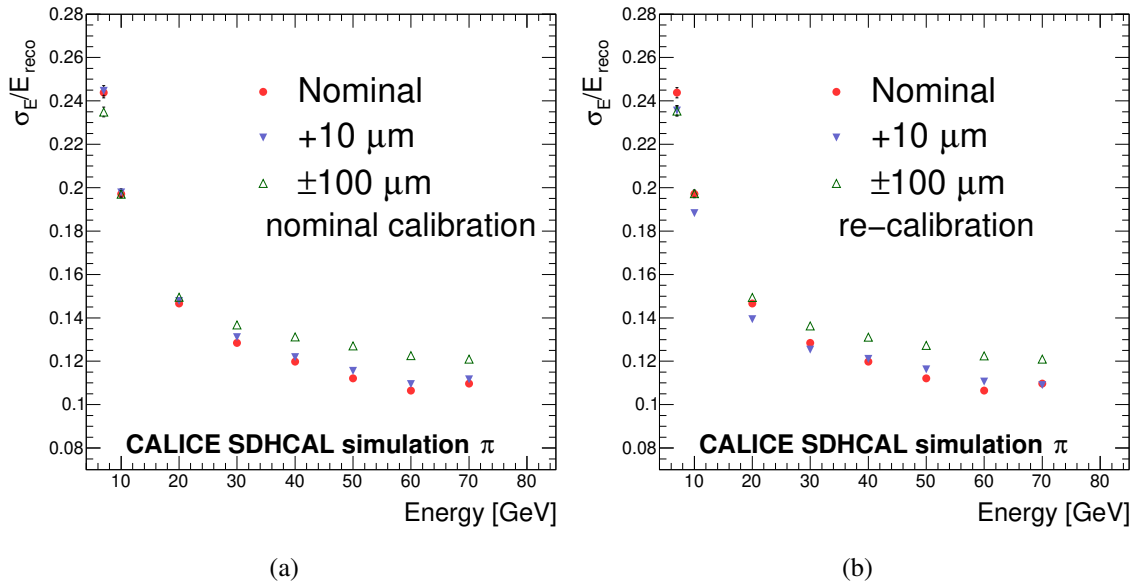
(a)   (b)

Figure 11: Relative energy resolution for pions versus generated energy for simulations using nominal gap (red circles), coherent gap variation by +10 μm (blue filled triangles) and random gap variation by ±100 μm (green open triangles). For each of the three simulation options, the energy reconstruction factors are (a) optimised using the nominal simulation for all cases or (b) re-calibrated for each geometry.

(a)	(b)
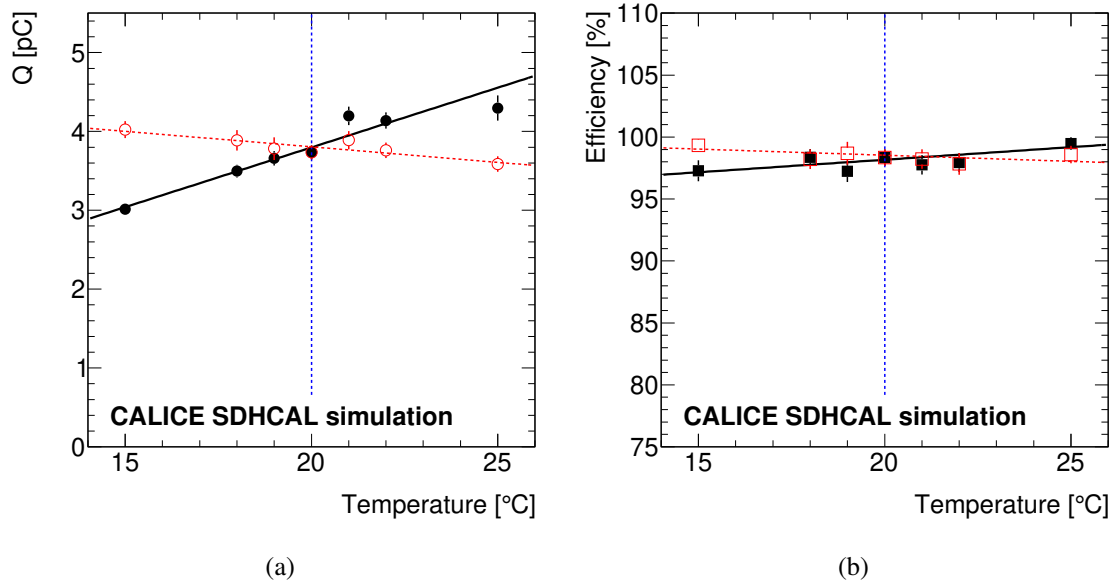
Figure 12: Mean total induced charge (a) and efficiency (b) as a function of the gas temperature for hits initiated by simulated 100 GeV muons. The nominal temperature is indicated by a vertical dashed blue line. High voltage is assumed to be stable (solid markers) or rescaled with the temperature (empty markers). The linear function that fits the variations is represented by a black solid line and a red dotted line.

5.3 Impact of temperature and pressure

At a given pressure, the temperature affects the gas density and therefore the charge multiplication and the absorption probabilities, charge velocity as well as the diffusion amplitude. The multiplication and absorption probabilities scale linearly with the temperature. In order to quantify the stability of the detector response in an evolving environment, the temperature and pressure are varied in the simulation as follows, starting with the variation of the temperature only first and assuming a stable high voltage. The amplitude and the efficiency of the signal are estimated and reported in Figures 12a and 12b. It is found that a drop of the temperature by 5°C is accompanied by an efficiency drop of 1% while the amplitude of the signal is reduced by 20%. These effects are propagated to the number of hits as shown in Figure 13.

The energy calibration reconstruction factors, a, b and c, are compared for pions in Figure 14 at three detector temperatures. The energy is reconstructed, using the nominal factors, from simulated events at different temperatures (see Figure 15). In the absence of re-calibration (Figure 15a), the reconstructed energy of a 40 GeV pion varies by 9% if the temperature is varied by 2°C. When the energy calibration reconstruction factors are adapted to each simulation (Figure 15b), the linearity of the energy is restored. The impact on the energy resolution was also checked. The relative energy resolution varies by less than one 1% if the temperature is varied by ±2°C as shown in Figure 16

A similar study is performed by varying the atmospheric pressure in the simulation. The amplitude of the signal and the efficiency are estimated for different GRPC gas pressures and
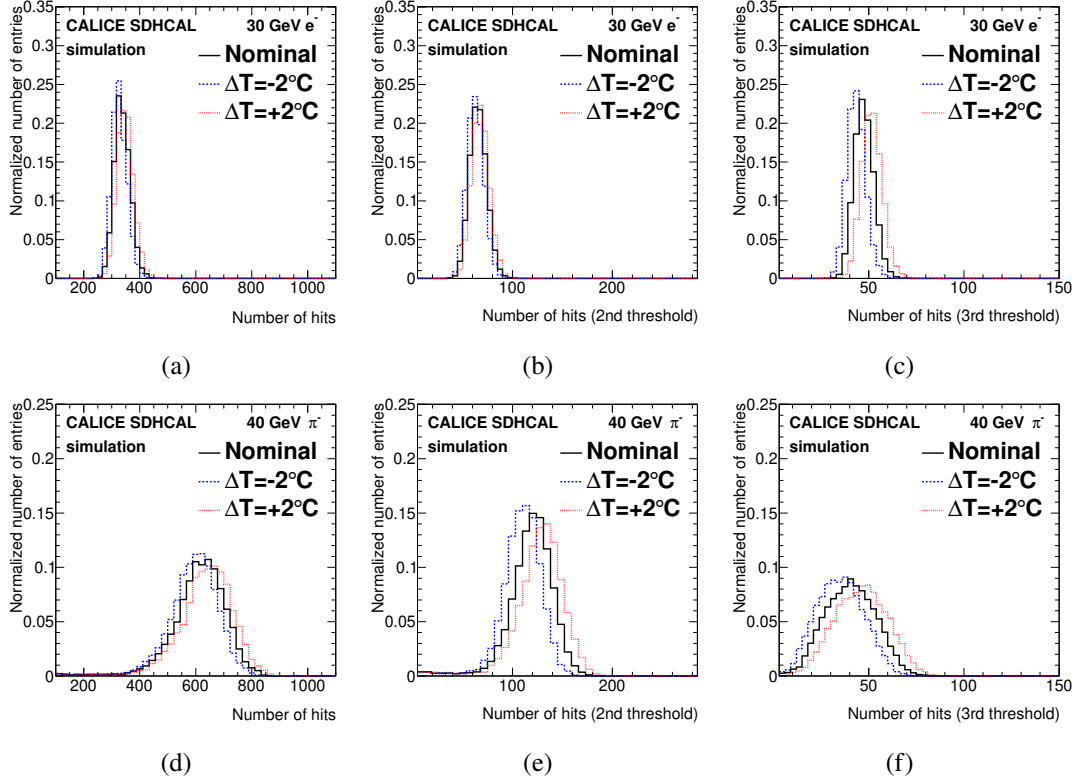
Figure 13: Distribution of the number of hits passing the first threshold at 0.1 pC (a,d), the second threshold at 5 pC (b,e) and the third threshold at 15 pC (c,f) for simulated 30 GeV electrons (top) or 40 GeV pions (bottom). The full GEANT4 simulation was performed with digitization modeling using the nominal temperature (solid black histograms), using a temperature varied by $-2°$C (dashed blue histogram) or $+2°$C (dotted red histogram).

reported in Figures 17a and 17b. A typical pressure increase of 10 mbar is accompanied by a total induced charge decrease of 11% and an efficiency loss below 1%. This trend is included in the digitizer algorithm.

The dependence of the number of hits to a pressure variation is illustrated in Figure 18. A pressure increase of 10 mbar leads to a variation of the average number of hits of -4.5%. The energy is reconstructed using the nominal factors and applied to simulated samples assuming different gas pressures. In this case the reconstructed energy of 40 GeV pions is biased by 12%. When the energy calibration reconstruction factors are optimised on each simulation, the energy linearity is improved as shown in Figure 19.

It was previously shown that adjusting the applied high voltage, V, by a value ΔV such as

$$\Delta V / V = \Delta T / T \tag{5.3}$$

where $\Delta T / T$ is the relative temperature variation, allows maintaining an approximately stable efficiency [23]. The simulation is used to test the efficiency of this method.
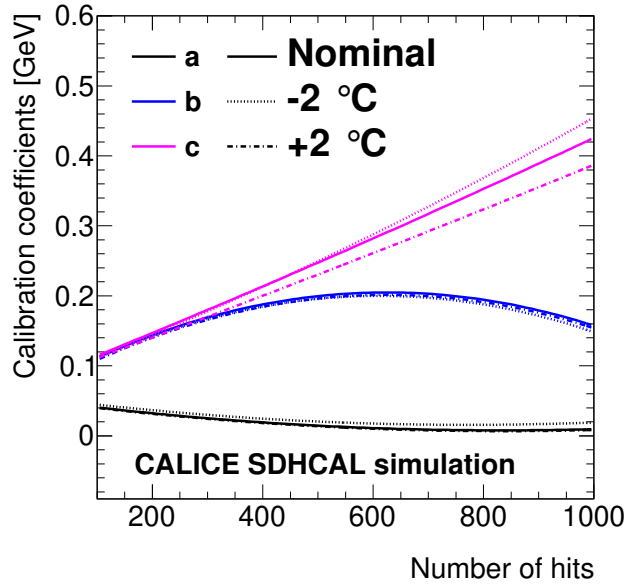
Figure 14: Dependences of the *a*, *b* and *c* energy calibration reconstruction factors on the number of hits. The factors are determined from a simulated sample of pion showers with the GRPCs at the nominal temperature (solid lines), a variation of −2°C (dotted lines) and +2°C (dash-dotted lines).

A dedicated simulation was performed where both temperature and the applied electric field amplitude are changed. It was assumed that the high voltage is scaled following eq. (5.3). As shown on Figure 12, the stability of the GRPC response is then improved by the high voltage tuning. The trends in the total induced charge and efficiency are reduced. However, a residual dependence to the temperature is observed in the simulation. A temperature increase of 5°C leads to a decrease of the total induced charge by 5.3% in a detector where the high voltage is scaled, whereas it would increase by 22% in a detector where the high voltage is constant.

The effect of the temperature on the GRPC signal is linear while a non-linear dependence to the high voltage is expected as reported in ref. [24]. An online automatized high voltage adjustment would require a tuning specific to this detector.

5.4 Impact of magnetic field

The SDHCAL technology proposal intends to equip a full-size hadronic calorimeter in a large scale detector like ILD. In this context, it has to be operated under a strong magnetic field of a few Tesla. The magnetic field affects the electron attachment and multiplication coefficients in the GRPC as well as their velocity and diffusion length. The Townsend coefficients, the diffusion length and the electron velocity are stable within 1 to 3% when the magnetic field is increased from 0 to 4 Tesla. Two magnetic field configurations are considered: perpendicular and longitudinal to the GRPCs as expected in the forward and barrel regions.

Events induced by 100 GeV muons are produced under different magnetic field configurations. The total induced charge and efficiency are given as a function of the amplitude of a longitudinal
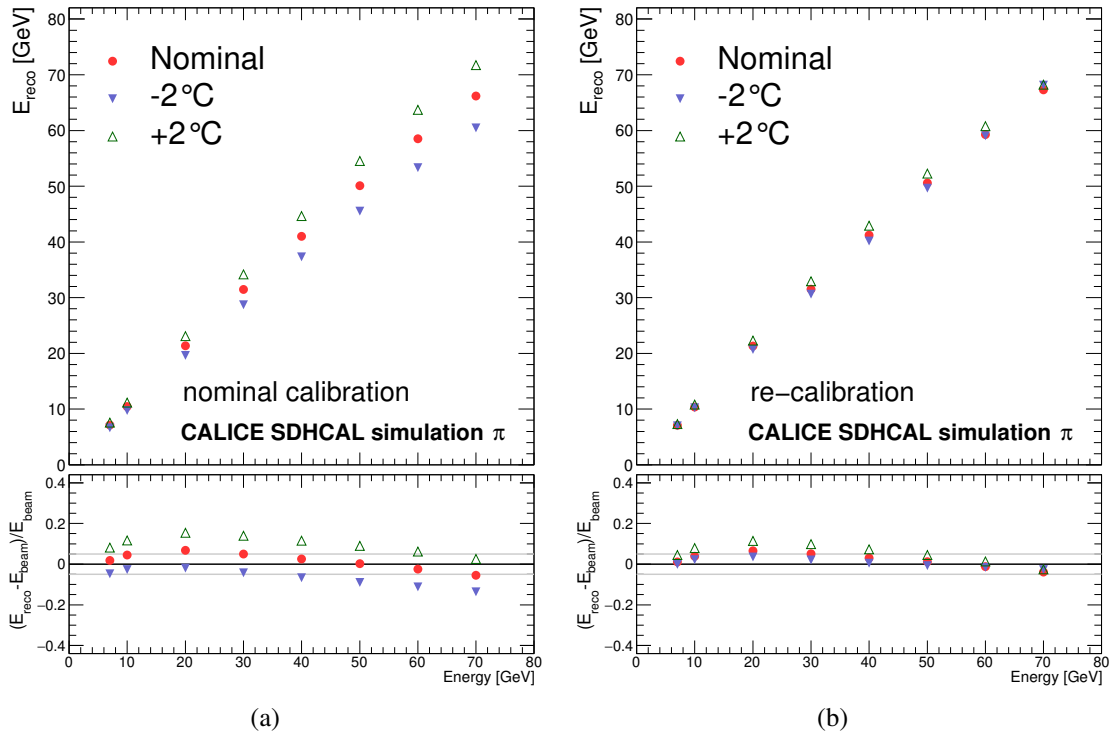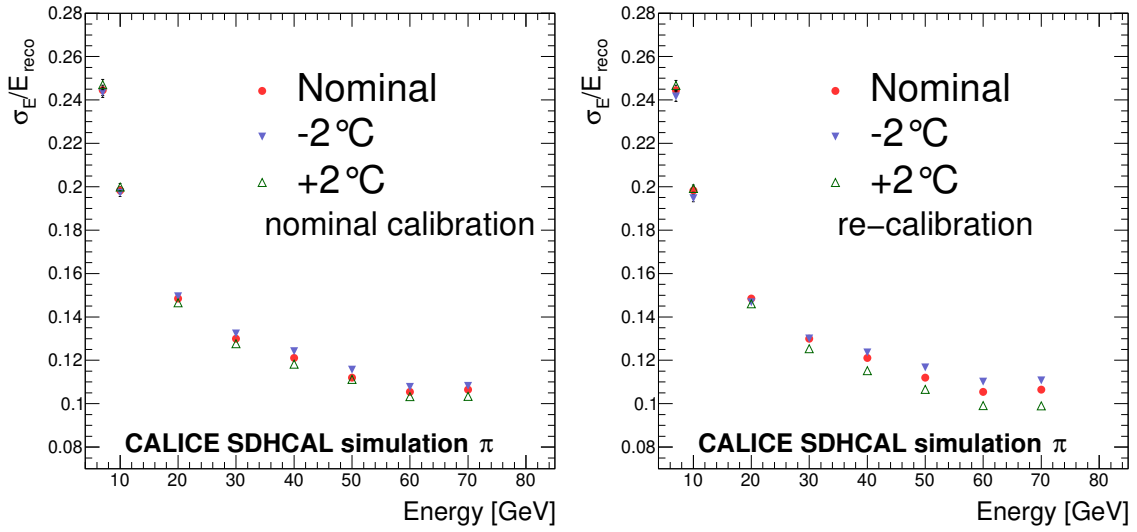
Figure 15: Pion reconstructed energy as a function of the generated energy for simulations with the GRPCs at the nominal temperature (red circles), a temperature variation by $-2°$C (blue filled triangles) and $+2°$C (green open triangles). The energy calibration reconstruction factors are calibrated using the nominal simulation for all cases (a) or re-calibrated for each of the three simulations (b).
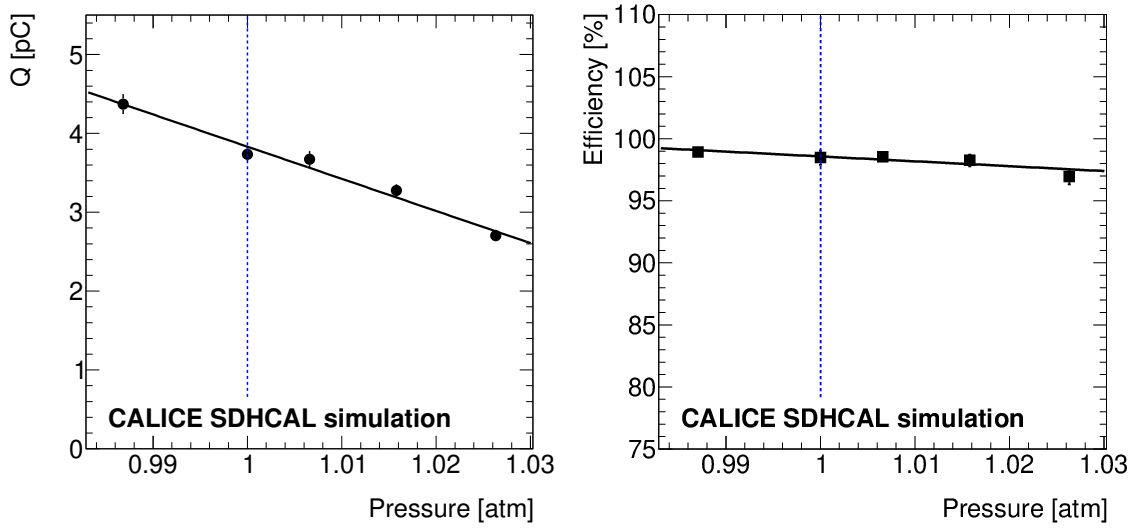
field on Figures 20a and 20b. No significant effect on the GRPC performances is observed at the hit level. This agrees with the test reported in ref. [6]. Thus no dependence on the magnetic field is implemented in the digitizer algorithm.

Figure 16: Relative energy resolution for pions versus generated energy for simulations with GRPCs at the nominal temperature (red circles), a temperature variation by $-2°C$ (blue filled triangles) and $+2°C$ (green open triangles). The energy reconstruction factors are optimised using the nominal simulation for all cases (a) or re-calibrated for each of the three simulation options (b).

Figure 17: Mean total induced charge (a) and efficiency (b) as a function of the gas pressure for hits initiated by simulated 100 GeV muons. The nominal pressure is indicated by a vertical dashed blue line. The linear function that fits to the variations is represented by a black solid line.
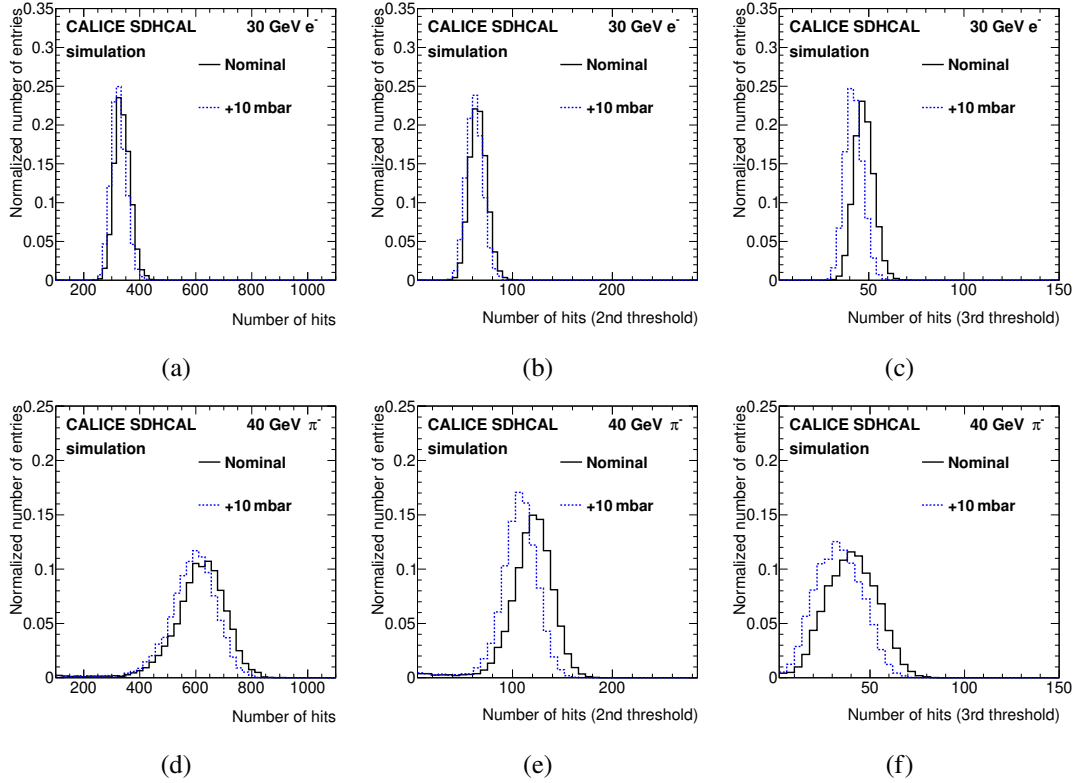
Figure 18: Distribution of the number of hits passing the first threshold at 0.1 pC (a,d), the second threshold at 5 pC (b,e) and the third threshold at 15 pC (c,f) for simulated 30 GeV electrons (top) or 40 GeV pions (bottom). The full GEANT4 simulation was performed with digitization modeling using the nominal pressure (solid black histograms) or a modeling where the pressure is increased by +10 mbar (dashed blue histogram).
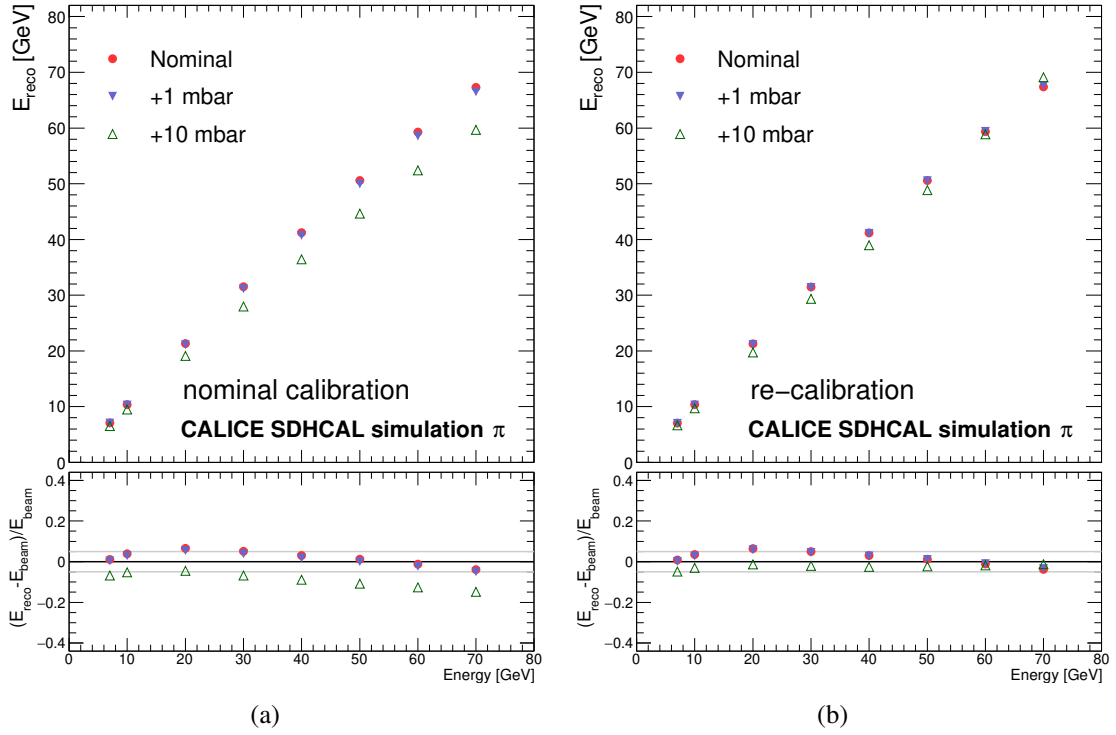
Figure 19: Pion reconstructed energy as a function of the generated energy for simulations with the GRPCs at the nominal pressure (red circles) and a pressure variation by +10 mbar (blue filled triangles). The energy reconstruction factors are calibrated using the nominal simulation for all cases (a) or re-calibrated for each of the three simulations (b).
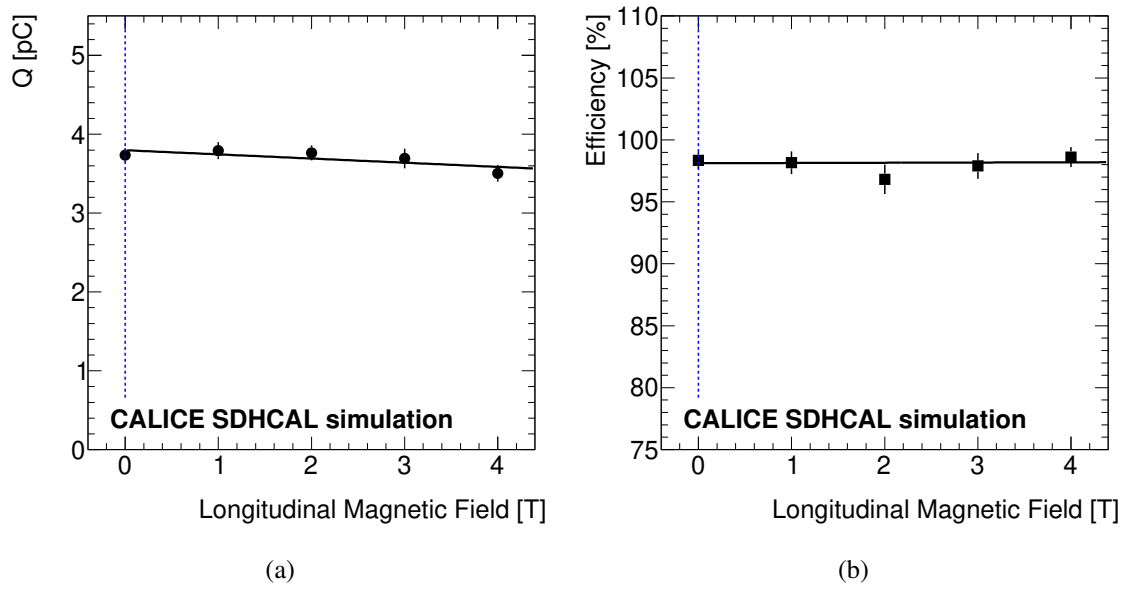
(a)

(b)

Figure 20: Mean total induced charge (a) and efficiency (b) as a function of the magnetic field amplitude, longitunidal to the GRPC, for hits initiated by simulated 100 GeV muons. The nominal magnetic field amplitude in the simulation is indicated by a vertical dashed blue line. The linear function that fits the variation is shown with a solid line.
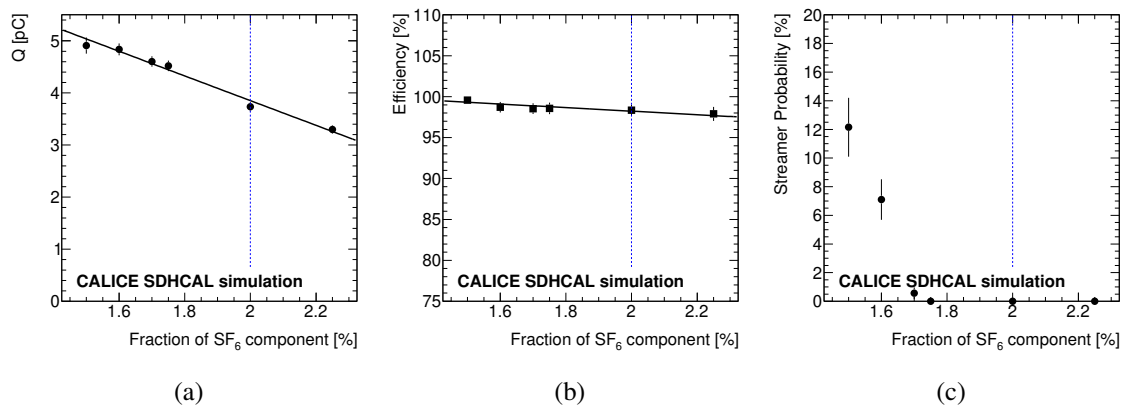
(a)   (b)   (c)

Figure 21: Mean total induced charge (a), efficiency (b) and streamer probability (c) as a function of the fraction of SF_6 for hits initiated by simulated 100 GeV muons. The nominal SF_6 fraction is indicated by a vertical dashed blue line. The linear function that fits to the variation is represented by a black solid line.

5.5 Impact of gas mixture

A composition of the gas mixture combined to the high voltage is at the core of the amplification process. Variations in the gas mixture lead to changes on the gain. The fractions of SF_6 and CO_2 components were varied and the expected signal and efficiencies are estimated for different fractions. In the following, a variation of 5% in SF_6 was considered for the stability study. This variation is considered as pessimistic compared to the precision of typical flowmeters used to control the gaz mixture which is 0.6% [25].

It is found that the total induced charge drops by 6% if the amount of SF_6 is varied by 5% (which corresponds to the variation in the total SF_6 fraction by 0.1%), while the efficiency is also reduced (cf. Figure 21). A reduction of SF_6 is accompanied by an increase of the high charge probability that is interpreted as an increased risk of streamers as seen in Figure 21c. This effect was implemented in the digitizer algorithm and used in full GEANT4 simulations of electron and pion showers.

This effect leads to a variation in the number of hits as shown in Figure 22. The impact on the energy reconstruction was studied using the same approach as described in the previous sections. The energy is reconstructed, using the nominal factors and from simulated events with different SF_6 fractions. It is shown in Figure 23 that in the absence of re-calibration, the reconstructed energy of a 40 GeV pion varies by ±20% if the relative amount SF_6 is varied by ∓5%.

For a relative variation of ±20% of the CO_2 component, i.e. between 4 and 6% of the gas mixture, no significant effect is observed within the precision of the simulation. However, the full impact of CO_2, especially on secondary avalanches, is not modeled in this simulation.
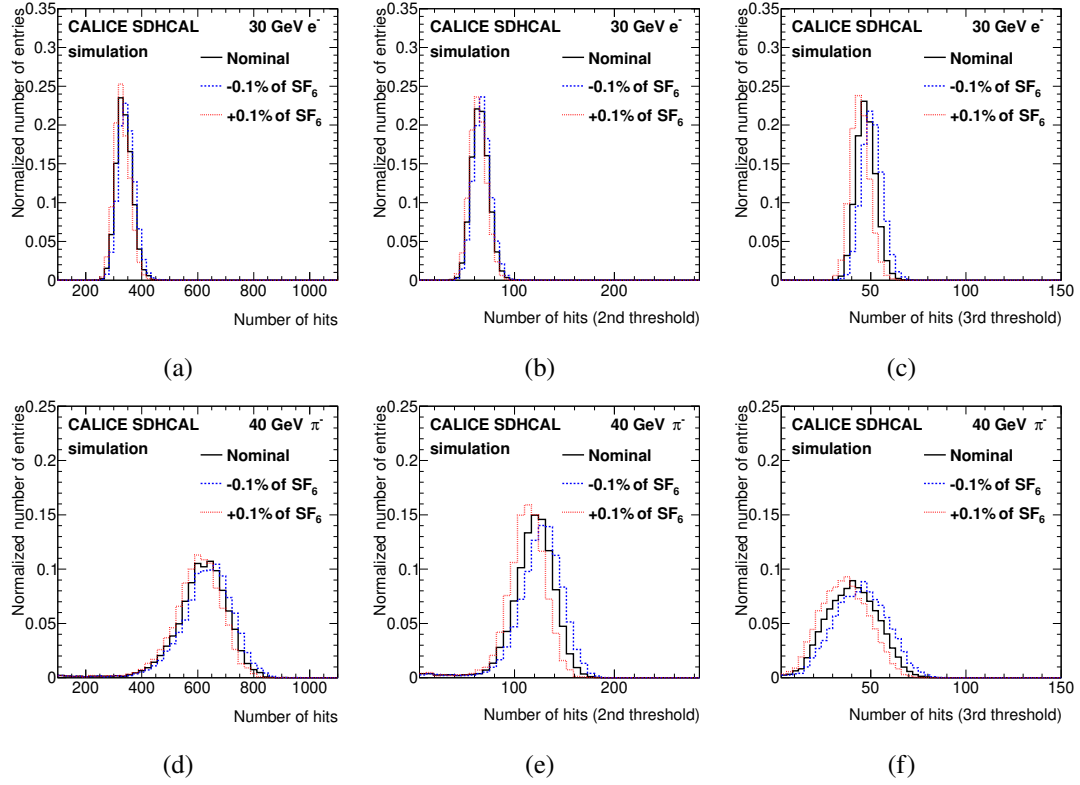
Figure 22: Distribution of the number of hits passing the first threshold at 0.1 pC (a,d), the second threshold at 5 pC (b,e) and the third threshold at 15 pC (c,f) for simulated 30 GeV electrons (top) or 40 GeV pions (bottom). The full GEANT4 simulation was performed with digitization modeling using the nominal SF_6 component fraction (solid black histograms) and the SF_6 fraction decreased by 0.1% (dashed blue histogram) or increased by 0.1% (dotted red histogram).
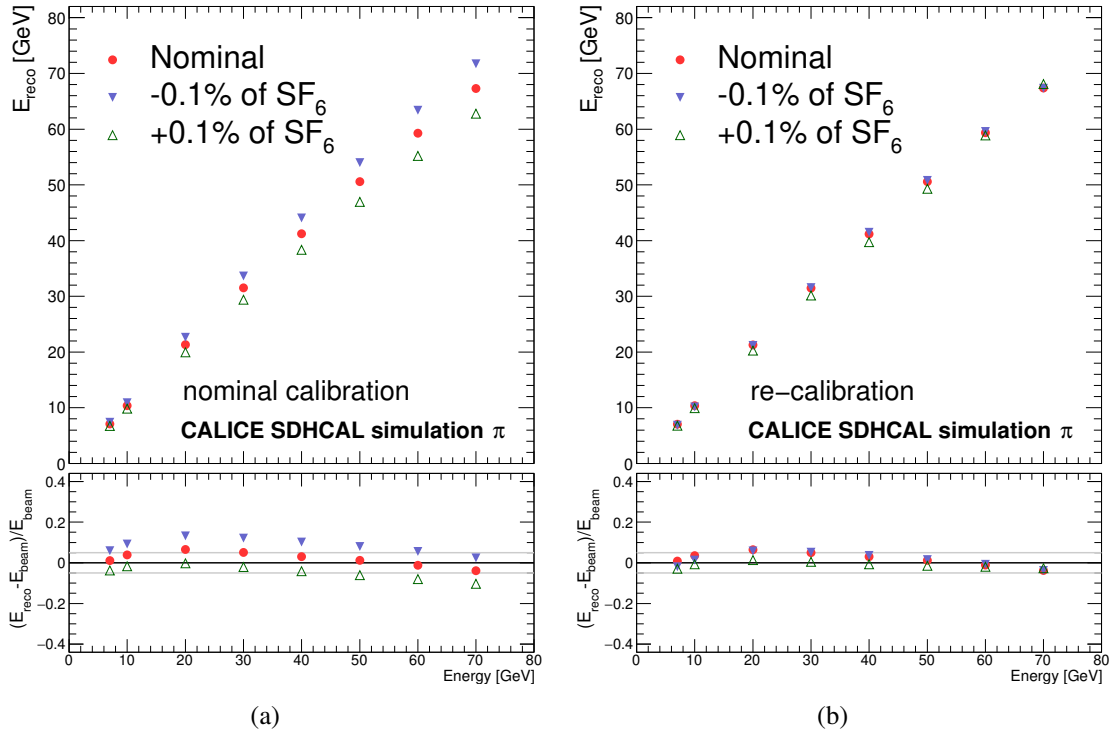
Figure 23: Pion reconstructed energy as a function of the generated energy for simulations with the GRPCs using the nominal SF_6 component fraction (red circles), the SF_6 component fraction decreased by 0.1% (blue filled triangles) and increased by +0.1% (green open triangles). The energy calibration reconstruction factors are optimized using the nominal simulation for all cases (a) or re-calibrated for each of the three simulations (b).

Table 2: Most significant effects and their corresponding impact on the detector response to 40 GeV pions. $\Delta Q/Q$ is the relative bias of the single MIP induced charge with respect to its nominal value. $\Delta N_{\text{tot}}/N_{\text{tot}}$ is the variation in the total number of hits. $\Delta N_2/N_2$ is the variation in the number of hits passing the second threshold, and $\Delta N_3/N_3$ for the number of hits passing the third threshold. $\Delta E/E$ is the relative bias of the reconstructed energy when applying an energy reconstruction defined on the nominal detector simulation to simulated data at different conditions.

		$\Delta Q/Q$ [%]	$\Delta N_{\text{tot}}/N_{\text{tot}}$ [%]	$\Delta N_2/N_2$ [%]	$\Delta N_3/N_3$ [%]	$\Delta E/E$ [%]
Gap	$+10\,\mu m$	-7.2 ± 0.3	-3.5 ± 0.2	-8.0 ± 0.3	-12.3 ± 0.5	-8.6 ± 0.5
	$\pm 100\,\mu m$		-7.9 ± 0.2	-13.7 ± 1.8	-19.2 ± 0.2	-6.9 ± 0.2
T	$+1^{\circ}C$	4.1 ± 0.4	1.9 ± 0.2	4.3 ± 0.4	7.5 ± 0.7	4.2 ± 1.1
P	$+10\,mbar$	-11.1 ± 0.9	-4.5 ± 0.3	-11.3 ± 0.4	-18.7 ± 0.9	-11.9 ± 0.8
SF$_6$	$+5\%$	-6.4 ± 0.4	-2.8 ± 0.2	-6.5 ± 0.2	-11.6 ± 0.2	-7.2 ± 0.7

5.6 Summary of detector effects simulation

The dependence of the detector response on the initial ionizing particle was described and included in the digitization procedure. It was shown that a magnetic field has no significant impact on the SDHCAL performance. However, other scenarios tested in the simulation can lead to non negligible effects as summarized in Table 2. The uncertainties on the variation in the number of hits correspond to the finite Monte Carlo size and to the uncertainty on the total induced charge variation. It is also checked that in the situation where these effects are definite and known, e.g. a static detector deformation, updating the energy calibration factors for each homogeneous data sample allows to restore the linearity of detector response with some resolution loss. A simulation that is tuned with beam test data (e.g. muon events to tune the charge distribution) in a given condition of temperature, pressure or mechanical homogeneity will wrongly model the data collected under different conditions, both in terms of amplitude and resolution.

6 Comparison with Beam Test Data

Among all the effects that can induce a sizable variation in the detector response, temperature, pressure and gap width variation were classified as the most significant ones. The test beam data collected in 2015 allow correlating the detector response with the temperature or pressure. However, the experimental setup cannot provide monitoring of the mechanical structure at a scale of $10\,\mu m$. Furthermore, the high voltage was adjusted in some data-taking periods.

In this section, a period where the high voltage was stable is considered. The prototype was exposed to a beam of pions at six different energies. Trends are observed within the runs and are associated with changes in the temperature or pressure and unstable beam intensities that lead to evolving saturations during the run. The temperature was measured at the outer side of three chambers which can lead to a bias with respect to the actual GRPC gas temperature. The largest temperature difference between two runs is $2.1^{\circ}C$. The atmospheric pressure was measured and the largest difference between two runs is 0.6 mbar.

The linearity of the detector response is compared to the simulated one, as seen in Figure 24. Two simulations were used in Figure 24a. In the first one, stable data-taking conditions were
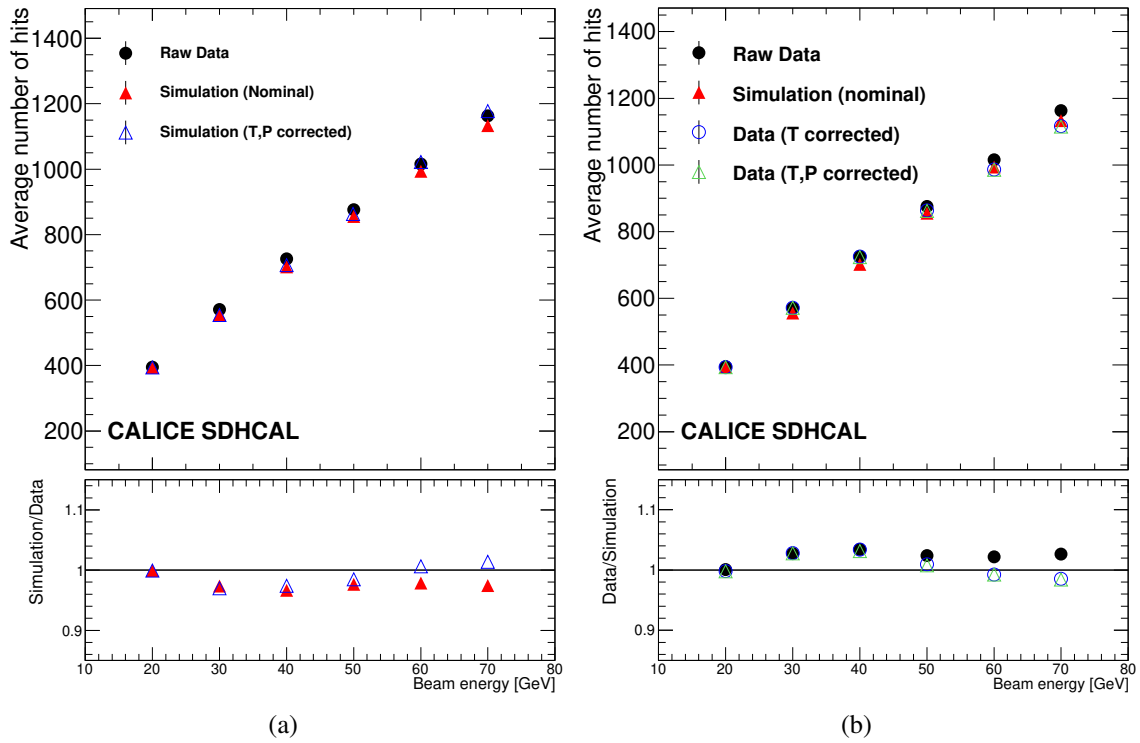
Figure 24: (a) Evolution of the number of hits as a function of the pion beam energy. Uncorrected data (black dots) are compared to the nominal simulation that assumes stable data taking conditions (full red triangles) and to a simulation including the observed temperatures and pressures (empty triangles). (b) An event by event correction is applied to the data (black circles) in order to compensate for temperature variations (empty circles), temperature and pressure variations (empty triangles), compared to the nominal simulation (full red triangles).

considered. The second simulated sample was produced using the average observed temperature and pressure, run by run, as input leading to a better agreement.

Although the purpose of the simulation is to predict the stability of the detector and not to correct the data, the overall impact of the temperature on the detector response was also checked by including an event by event correction to the number of hits. This correction is deduced from the simulation and is a function of the temperature and of the pressure associated to the event.

The correction improves the agreement between data and simulation as seen on Figure 24b.

Among all the simulated effects presented in this document, only the gap inflation can produce random layer-to-layer variations in the detector response. The efficiency was estimated from simulated and observed pion showers using reconstructed tracks. The layer efficiencies are reported in Figure 25. The digitizer algorithm accounts for the overall observed efficiency but does not include any data-driven mapping of it. It was assumed that the charge collection and readout is homogeneous. The layer-to-layer variations observed in the nominal simulation are due to statistical fluctuations. Simulating a $\pm 100\,\mu m$ gap width tolerance introduces a sizable spread in the efficiency. However, this spread is still smaller than what is observed in the data. The layer-to-layer variations
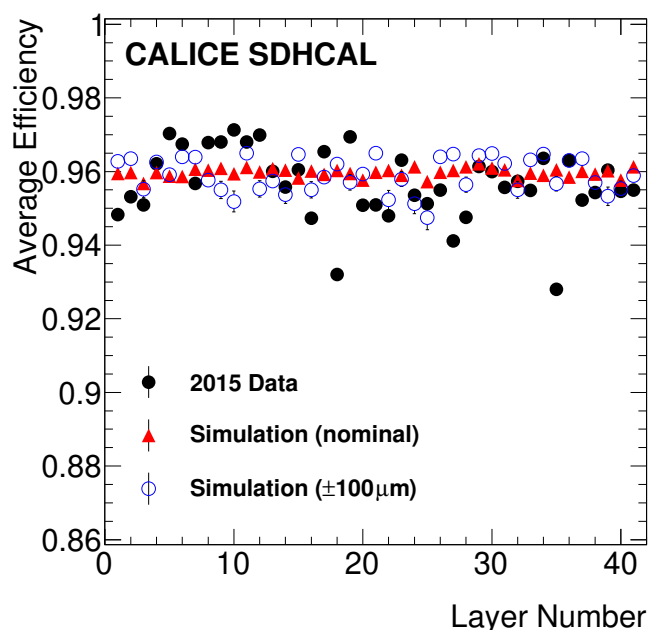
Figure 25: Average efficiency estimated for each layer of the SDHCAL prototype using beam test data (black filled circles), simulation with digitization modeling using the nominal geometry (red triangles) and a geometry where the gaps are randomly varied within ±100 μm (blue open circles).

observed in the data reflects the inhomogeneity of the gap widths superimposed with potential other effects not modeled in this study, like dead channels, inhomogeneous readout or inhomogeneous layer paintings.

7 Conclusion

The SDHCAL digitizer algorithm was extended to include dependencies on the particle types, temperature, pressure, gap width deformations, magnetic field and gas mixture changes. It was used to model the detector response, including different scenarios. It was shown that when the SDHCAL technology is used with a purely digital approach, its key performances are quite stable regarding data-taking conditions and potential detector inhomogeneities. The detector efficiency variation is at the percent level while the typical variation in the total number of hits is smaller than 5%. When exploiting the semi-digital information, its performances are affected, especially when the detector is confronted with mechanical or temperature variations. However, it was also shown that the energy linearity could be restored via frequent calibrations with data. Online detector-based corrections were also implemented by changing the high voltage to mitigate some environmental effects like temperature and pressure variations. The performances of these corrections need to be studied.

8 Acknowledgements

References

[1] G. Baulieu et al. Construction and commissioning of a technological prototype of a high-granularity semi-digital hadronic calorimeter. *JINST*, 10(10):P10039, 2015.

[2] J.C. Brient. Improving the jet reconstruction with the particle flow method: An introduction. In *11th International Conference on Calorimetry in High-Energy Physics (Calor 2004)*, pages 445–451, 3 2004.

[3] Z. Deng et al. Tracking within Hadronic Showers in the CALICE SDHCAL prototype using a Hough Transform Technique. *JINST*, 12(05):P05009, 2017.

[4] D. Boumediene et al. Particle identification using Boosted Decision Trees in the Semi-Digital Hadronic Calorimeter prototype. *JINST*, 15(10):P10009, 2020.

[5] F. Dulucq et al. HARDROC: Readout chip for CALICE/EUDET Digital Hadronic Calorimeter. In *2010 IEEE Nuclear Science Symposium, Medical Imaging Conference, and 17th Room Temperature Semiconductor Detectors Workshop*, pages 1678–1683, 2010.

[6] L. Caponetto et al. First test of a power-pulsed electronics system on a GRPC detector in a 3-Tesla magnetic field. *JINST*, 7:P04009, 2012.

[7] Ties Behnke, James E. Brau, Brian Foster, Juan Fuster, Mike Harrison, James McEwan Paterson, Michael Peskin, Marcel Stanitzki, Nicholas Walker, and Hitoshi Yamamoto. The international linear collider technical design report - volume 1: Executive summary, 2013.

[8] B. Bilki et al. Measurement of the rate capability of resistive plate chambers. *JINST*, 4(06):P06003, jun 2009.

[9] V. Buridon et al. First results of the CALICE SDHCAL technological prototype. *JINST*, 11(04):P04001, 2016.

[10] F. Gaede. Marlin and LCCD: Software tools for the ILC. *Nucl. Instrum. Meth. A*, 559:177–180, 2006.

[11] O. Wendt, F. Gaede, and T. Kramer. Event Reconstruction with MarlinReco at the ILC. *Pramana*, 69:1109–1114, 2007.

[12] ILC software portal, http://ilcsoft.desy.de.

[13] S. Agostinelli et al. GEANT4–a simulation toolkit. *Nucl. Instrum. Meth. A*, 506:250–303, 2003.

[14] Z. Deng et al. Resistive Plate Chamber Digitization in a Hadronic Shower Environment. *JINST*, 11(06):P06014, 2016.

[15] M. Abbrescia et al. The simulation of resistive plate chambers in avalanche mode: Charge spectra and efficiency. *Nucl. Instrum. Meth. A*, 431:413–427, 1999.

[16] V. Français. *Description and simulation of the physics of Resistive Plate Chambers*. PhD thesis, Laboratoire de Physique Corpusculaire - Clermont-Ferrand, France, 2017.

[17] V. Français. Description and simulation of physics of Resistive Plate Chambers. *JINST*, 11(05):C05023, 2016.

[18] I.B. Smirnov. Modeling of ionization produced by fast charged particles in gases. *Nucl. Instrum. Meth. A*, 554:474–493, 2005.

[19] W. Riegler, C. Lippmann, and R. Veenhof. Detector physics and simulation of resistive plate chambers. *Nucl. Instrum. Meth. A*, 500:144–162, 2003.

[20] S.F. Biagi. Monte Carlo simulation of electron drift and diffusion in counting gases under the influence of electric and magnetic fields. *Nucl. Instrum. Meth. A*, 421(1-2):234–240, 1999.

[21] R. Cardarelli, R. Santonico, and V. Makeev. Avalanche and streamer mode operation of resistive plate chambers. *Nucl. Instrum. Meth. A*, 382:470–474, 1996.

[22] H. Bethe. Theory of the Passage of Fast Corpuscular Rays Through Matter. *Annalen Phys.*, 5:325–400, 1930.

[23] M. Abbrescia et al. Resistive plate chambers performances at cosmic rays fluxes. *Nucl. Instrum. Meth. A*, 359:603–609, 1995.

[24] S. Colafranceschi et al. Performance of the Gas Gain Monitoring system of the CMS RPC muon detector and effective working point fine tuning. *PoS*, RPC2012:046, 2012.

[25] BROOKS Instrument. *Mass Flow Controllers & Meters, SLA5800 Series*, 5 2020.